

Overview of ASDEX Upgrade Results

U. Stroth, J. Adamek¹, L. Aho-Mantila², S. Äkäslompolo²,
C. Amdor⁶, C. Angioni, M. Balden, S. Bardin³, L. Barrera
Orte, K. Behler, E. Belonohy, A. Bergmann, M. Bernert,
R. Bilato, G. Birkenmeier, V. Bobkov, J. Boom⁴,
C. Bottereau²⁰, A. Bottino, F. Braun, S. Brezinsek¹³,
T. Brochard²¹, M. Brüdgam, A. Buhler, A. Burckhart,
F.J. Casson, A. Chankin, I. Chapman⁸, F. Clairet²⁰,
I.G.J. Classen⁴, J.W. Coenen¹³, G.D. Conway, D.P. Coster,
D. Curran¹⁷, F. da Silva⁶, P. de Marné, R. D’Inca, D. Douai²⁰,
R. Drube, M. Dunne¹⁷, R. Dux, T. Eich, H. Eixenberger,
N. Endstrasser, K. Engelhardt, B. Esposito⁵, E. Fable,
R. Fischer, H. Fünfgelder, J.C. Fuchs, K. Gál, M. García
Muñoz, B. Geiger, L. Giannone, T. Görler, S. da Graca⁶,
H. Greuner, O. Gruber, A. Gude, L. Guimarais⁶, S. Günter,
G. Haas, A.H. Hakola², D. Hangan, T. Happel, T. Härtl,
T. Hauff, B. Heinemann, A. Herrmann, J. Hobirk,
H. Höhnle¹⁰, M. Hölzl, C. Hopf, A. Houben, V. Igochine,
C. Ionita¹², A. Janzer, F. Jenko, M. Kantor, C.-P. Käsemann,
A. Kallenbach, S. Kálvin⁷, M. Kantor¹³, A. Kappatou⁴,
O. Kardaun, W. Kasperek¹⁰, M. Kaufmann, A. Kirk⁸,
H.-J.Klingshirn, M. Kocan, G. Kocsis⁷, C. Konz,
R. Koslowski¹³, K. Krieger, M. Kubic²⁰, T. Kurki-Suonio²,
B. Kurzan, K. Lackner, P.T. Lang, P. Lauber, M. Laux,
A. Lazaros²³, F. Leipold¹⁴, F. Leuterer, S. Lindig, S. Lisgo²⁰,
A. Lohs, T. Lunt, H. Maier, T. Makkonen, K. Mank,
M.-E. Manso⁵, M. Maraschek, M. Mayer, P.J. McCarthy¹⁷,
R. McDermott, F. Mehlmann¹², H. Meister, L. Menchero,
F. Meo¹⁴, P. Merkel, R. Merkel, V. Mertens, F. Merz,
A. Mlynek, F. Monaco, S. Müller¹⁹, H.W. Müller, M. München,
G. Neu, R. Neu, D. Neuwirth, M. Nocente¹⁵, B. Nold¹⁰,
J.-M. Noterdaeme, G. Pautasso, G. Pereverzev, B. Plöckl,
Y. Podoba, F. Pompon, E. Poli, K. Polozhiy, S. Potzel,
M.J. Püschel, T. Pütterich, S.K. Rathgeber, G. Raupp,
M. Reich, F. Reimold, T. Ribeiro, R. Riedl, V. Rohde,
G. v. Rooij⁴, J. Roth, M. Rott, F. Ryter, M. Salewski¹⁴,
J. Santos⁶, P. Sauter, A. Scarabosio, G. Schall, K. Schmid,

P.A. Schneider, W. Schneider, R. Schrittwieser¹², M. Schubert, J. Schweinzer, B. Scott, M. Sempf, M. Sertoli, M. Siccinio, B. Sieglin, A. Sigalov, A. Silva⁶, F. Sommer, A. Stähler, J. Stober, B. Streibl, E. Strumberger, K. Sugiyama, W. Suttrop, T. Tala², G. Tardini, M. Teschke, C. Tichmann, D. Told, W. Treutterer, M. Tsalas⁴, M. A. Van Zeeland⁹, P. Varela⁶, G. Veres⁷, J. Vicente⁶, N. Vianello¹⁶, T. Vierle, E. Viezzer, B. Viola¹⁶, C. Vorpahl, M. Wachowski²², D. Wagner, T. Wauters²⁰, A. Weller, R. Wenninger, B. Wieland, M. Willensdorfer¹⁸, M. Wischmeier, E. Wolfrum, E. Würsching, Q. Yu, I. Zammuto, D. Zasche, T. Zehetbauer, Y. Zhang, M. Zilker, H. Zohm

Max-Planck-Institut für Plasmaphysik, EURATOM-Association, Boltzmannstr. 2, 85748 Garching, Germany, ¹Institute of Plasma Physics, Praha, Czech Republic, ²Association EURATOM-Tekes, Helsinki, Finland, ³ Institute of Atomic Physics, EURATOM Association-MEdC, Romania, ⁴ FOM-Institute DIFFER, EURATOM Association, TEC, Nieuwegein, The Netherlands, ⁵ C.R.E ENEA Frascati, EURATOM Association, CP 65, 00044 Frascati, (Rome), Italy, ⁶ IPFN, EURATOM Association-IST Lisbon, Portugal, ⁷ KFKI, EURATOM Association-HAS, Budapest, Hungary, ⁸ EURATOM/CCFE Fusion Association, Culham Science Centre, UK, ⁹ General Atomics, San Diego, California, 92186-5608, USA, ¹⁰Institut für Plasmaphysik, Universität Stuttgart, Germany, ¹² University of Innsbruck, EURATOM Association-ÖAW, Austria, ¹³Forschungszentrum Jülich, EURATOM-Association, Inst. Energie & Klimaforschung, Plasmaphysik, D-52425 Jülich, Germany, ¹⁴Association EURATOM - DTU, Technical University of Denmark, Department of Physics, Risø Campus, DK-4000 Roskilde, Denmark, ¹⁵ EURATOM Association-ENEA, IFP, CNR, Milano, Italy, ¹⁶ Consorzio RFX, EURATOM Association-ENEA, Padova, Italy, ¹⁷ Physics Department, University College Cork, Association EURATOM-DCU, Ireland ¹⁸ IAP, TU Wien, EURATOM Association-ÖAW, Austria, ¹⁹ Dept. Mech. & Aerospace Eng. UCSD, 9500 Gilman Drive, La Jolla CA 92093, USA, ²⁰ CEA, Cadarache, France ²¹Institut Jean Lamour, UMR 7198 CNRS, Vandoeuvre, France, ²²Warsaw University of Technology, Pl. Politechniki 1, 00-661 Warsaw, Poland, ²³ National Technical University of Athens Association Euratom/Hellenic-Republic, Athens, Greece

Abstract. The medium size divertor tokamak ASDEX Upgrade (major and minor radii 1.65 and 0.5 m, respectively, magnetic field strength 2.5 T) possesses flexible shaping and versatile heating and current drive systems. Recently the technical capabilities were extended by increasing the ECRH power [1, 2], by installing 2×8 internal magnetic perturbation coils [3, 4], and by improving the ICRF compatibility with the tungsten wall [5]. With the perturbation coils, reliable suppression of large type-I ELMs could be demonstrated in a wide operational window, which opens up above a critical plasma pedestal density. The pellet fueling efficiency was observed to increase which gives access to H-mode discharges with peaked density profiles at line densities clearly exceeding the empirical Greenwald limit [6, 7]. Owing to the increased ECRH power of 4 MW, H-mode discharges could be studied in regimes with dominant electron heating and low plasma rotation velocities [8, 9], i.e. under conditions particularly relevant for ITER. The ion-pressure gradient and the neoclassical radial electric field emerge as key parameters for the transition [10]. Using the total simultaneously available heating power of 23 MW, high performance discharges have been carried out where feed-back controlled radiative cooling in the core and the divertor allowed the divertor peak power loads to be maintained below 5 MW/m^2 [11]. Under attached divertor conditions, a multi-device scaling expression for the power decay length was obtained which is independent of major radius and decreases with magnetic field resulting in a decay length of 1 mm for ITER [12, 13]. At higher densities and under partially detached conditions, however, a broadening of the decay length is observed. In discharges with density ramps up to the density limit, the divertor plasma shows a complex behavior with a localized high-density region in the inner divertor before the outer divertor detaches [14, 15]. Turbulent transport is studied in the core and the scrape-off layer. Discharges over a wide parameter range exhibit a close link between core momentum and density transport [16]. Consistent with gyro-kinetic calculations, the density gradient at half plasma radius determines the momentum transport through residual stress and thus the central toroidal rotation [17]. In the scrape-off layer a close comparison of probe data with a gyro-fluid code showed excellent agreement and points to the dominance of drift waves [18]. Intermittent structures from ELMs and from turbulence are shown to have high ion temperatures even at large distances outside the separatrix [19, 20].

1. Introduction and technical boundary conditions

The main objective of the ASDEX Upgrade programme is to develop integrated scenarios for long-pulse operation of burning plasmas in ITER and DEMO which include solutions for plasma shaping, confinement and stability, divertor and power exhaust, as well as the choice of appropriate wall materials. This effort includes advancing the physical understanding of related fundamental problems in order to create reliable predicting capabilities and to discover new paths to advanced plasma operation. To reach these goals, ASDEX Upgrade is realized as a flexible device with versatile heating systems and excellent diagnostics. Plasma shape and divertor configurations are close to those of ITER and in a path-breaking effort tungsten has been qualified as a possible solution for the divertor and first wall material [21, 22]. In 2011 and 2012 systems for the control of plasma stability and the mitigation of damages possibly caused by the plasma have been improved. Systems for the real-time control of the plasma position by reflectometry [23],

of the divertor power load by impurity radiation [11], of neoclassical tearing modes by external current drive [24], and of disruptions by massive gas puffing [25] have been put in place and 2×8 internal magnetic perturbation coils are now used to mitigate large edge localized modes (ELMs) [26]. Disruption mitigation studies using massive gas injection showed an improved fueling efficiency of up to a factor of 2, when the valve is located on the high-field side [25]. The ECRH power has been increased to 4 MW and it was demonstrated that replacing NBI by ECRH or ICRH power leads to comparable global plasma parameters [27, 2] with the benefit for transport studies to change momentum and particle sources and the ratio of electron to ion temperature in the core. The ICRH system was improved [5] by installing a modified broad-limiter antenna, which reduced the rise in the tungsten concentration in the plasma during ICRH by up to 40% and substantially lowered the tungsten sputtering yield at the antenna limiters, and by replacing tungsten-coated antenna side limiters by boron-coated ones on two other antennas.

2. High-performance discharges

Power exhaust is a key concern on the way to a fusion reactor and the demonstration of stable high-performance discharges with acceptable divertor power loads is an important task for present day devices [11]. In order to keep the power on divertor targets below the required limit of 5 MW/m^2 , radiative cooling induced by injected impurities is used. In ASDEX Upgrade, the technique of feed-back controlled radiative cooling has been substantially advanced and applied to high-power discharges. By puffing argon into the main chamber, about 67% of the heating power of 23 MW could be radiated in the outer core plasma without degrading the confinement properties. In addition, nitrogen was injected from the divertor roof baffle in order to further reduce the power load on the divertor plates leading to radiation losses of about 5 MW from the divertor and X-point regions [11]. These discharges could be operated with a power load well below the limit expected for a reactor of 5 MW/m^2 which has to be compared with a value of 110 MW/m^2 as obtained from the applied $P/R = 14 \text{ MW/m}$ and a radial strike-line width of about 2 cm on the target. At the same time, with 9 MW the power flux across the separatrix stayed well above the threshold for the L-H transition.

Figure 1 shows the time traces of such a discharge which became possible through a real-time feedback system to independently monitor core and divertor radiation [28] through bolometry and a target temperature estimate, respectively. The maximum heating power of 23 MW is a mix of 17.5 MW of NBI, 4.5 MW of ICRH and, to limit tungsten accumulation in the plasma center, 1.5 MW of ECRH, which is injected in the second-harmonic ordinary (O2) mode, a heating scheme developed earlier [29]. The line-averaged density was close to the ITER value of 10^{20} m^{-3} and a high confinement factor of $H_{98} = 1$ and a normalized beta of $\beta_N = 3$ were maintained stationary over many energy confinement times. At the same time, the tungsten and argon concentrations stayed at the low values of $c_W = 2 \times 10^{-5}$ and $c_{Ar} = 3 \times 10^{-3}$ with $Z_{eff} \approx 2$. The

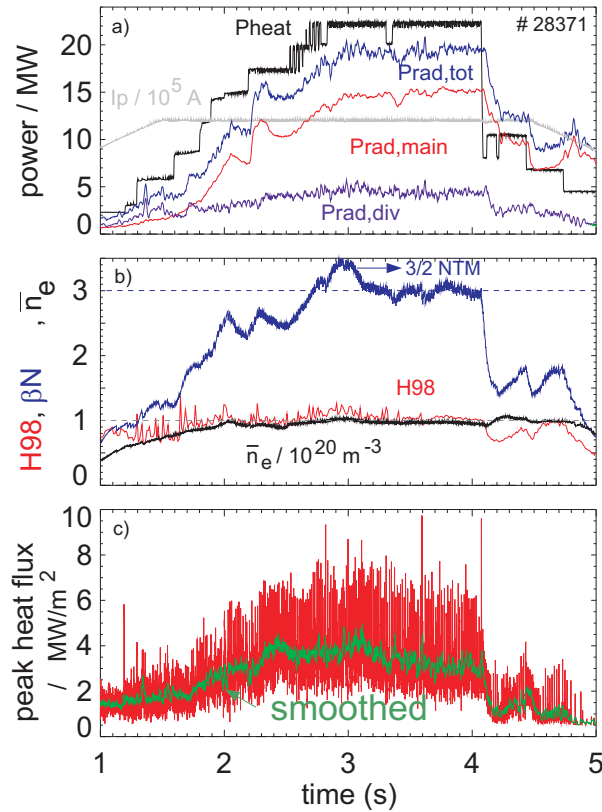


Figure 1. High performance discharge with feedback controlled double radiative cooling with argon and nitrogen (from Ref. [11]).

slight drop in β_N at about 3 s is attributed to a 3/2 neoclassical tearing mode (NTM). These results suggest that the combination of high main-chamber radiation and further increased divertor radiation will allow to control discharges at even higher values of P/R [11]. This will be demonstrated once higher heating power will be available on ASDEX Upgrade.

In high performance plasmas, neoclassical tearing modes can limit the accessible values of β_N . On ASDEX Upgrade, a closed-loop real-time feedback control system for NTM stabilization has been commissioned including mode detection, power deposition calculation and deposition control using a steerable ECRH mirror. For the experiments, a target plasma with 13 MW of external heating leading to $\beta_N = 2.7$ was used. On developing $m = 3$, $n = 2$ modes the functionality of the feed-back system was demonstrated and the mode amplitude could be reduced by means of localized electron-cyclotron current drive [24]. A complete stabilization was not yet achieved in all cases with only one gyrotron included in the feed-back loop. Demonstration of complete stabilization using several gyrotrons will be studied in the future.

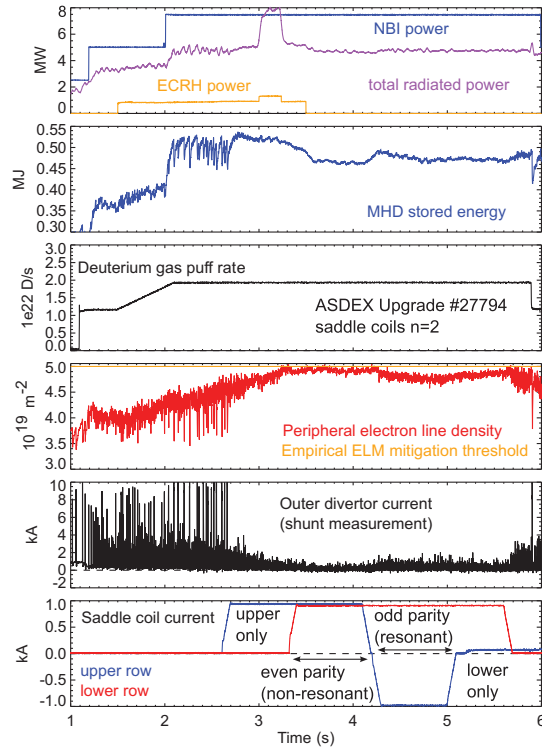


Figure 2. ELM mitigation with a $n = 2$ perturbation field comparing even (non-resonant) and odd (resonant) coil parity with single (upper and lower) row operation. (From Ref. [26]).

3. ELM mitigation with perturbation coils

In order to study the mitigation of the high divertor power loads on the divertor plates caused by ELMs, two rows of 8 saddle coils have been installed on ASDEX Upgrade. The coils allow for magnetic field perturbations with toroidal mode numbers $n \leq 4$. In a first step, with a reduced set of 2×4 coils only, it was demonstrated that type-I ELMs could be replaced by smaller and benign MHD events which appear at higher frequency [3]. Although these events resemble type-III ELMs, they are probably not since they do not show a precursor and they appear at pedestal temperatures well above 300 eV which is the upper limit for the appearance of type-III ELMs. A more detailed characterization is ongoing. The suppression of the type-I ELMs appears above a density threshold at about 65% of the Greenwald density limit. With the full set of 2×8 coils it became possible to study the influence of the toroidal mode number on ELM mitigation [26, 30]. For these studies, type-I ELMy H-Mode discharges heated by NBI were used.

Figure 2 shows a typical discharge where the density was ramped up and with the switch-on of the perturbation coil current, the large ELMs disappear. The effect does not depend on the phasing of the coils with respect to the resonance of the perturbation field with the background field. The suppression holds with only one of the coil rings active and with all coils phased in a resonant or non-resonant way. In Ref. [3] it was already shown that for $n = 2$ configurations, the resonance condition is not important

for ELM suppression. The validity of this results could now be extended to $n = 1$ and $n = 4$ magnetic-field perturbations [26]. Due to low local magnetic shear at the outboard midplane, the choice of the resonance condition is a global one, which holds simultaneously in a large radial range.

The ELMs are replaced by repetitive small scale MHD events, which cause lower energy losses but are sufficient to keep the tungsten concentration in the core plasma at a low level. The temperature in the outer divertor rises moderately during ELM mitigation but the inner divertor remains detached.

These investigations show that in ASDEX Upgrade ELM mitigation can be achieved with perturbations of different toroidal mode numbers and that it does not depend on a dominant resonant perturbation field component. ELM mitigation was also successful in plasmas with different heating schemes, different momentum input and thus different plasma rotation velocities [30]. In all cases, ELM mitigation is found only at a relatively high pedestal density. At the same time, collisionality does not appear to be an ordering parameter for the transition into the mitigated state.

Although having a strong influence on the ELMs, the field perturbations do not substantially affect the H-mode pedestal profiles and do not cause modes to grow and lock; also existing tearing modes do not lock to the error field in H-mode plasmas. This indicates, that the perturbation field is rather well screened by the plasma. Quantitative studies of error field penetration in the edge plasma are under way. Nevertheless, there is a mild sensitivity of the edge plasma density to the field configuration. Perturbations with $n = 1$ cause a reduction or an increase of about 10% in the resonant and non-resonant configuration, respectively. Indications for stronger effects of the field perturbations are, however, observed at lower densities and safety factors [31].

In the scrape-off layer (SOL) the calculated 3D vacuum field topology, as calculated by the EMC3 code [32], reproduces the patterns and the strike-line splitting measured on the target plates by means of IR cameras and Langmuir probes [33, 34]. Hence although there is little sign of a penetration of the error fields into the edge plasma, the modification of the field in the SOL region is clearly present and consistent with vacuum-field calculations. Further effects of the perturbation coils on the scrape-off layer are addressed Ref. [20].

A further beneficial effect of the applied field perturbations is that pellets do not trigger ELMs as they do in normal H-mode discharges. This opens again the possibility of pellet fueling with high efficiency. Injecting pellets from the high-field side of ASDEX Upgrade into ELM mitigated H-mode discharges leads to centrally peaked density profiles and line-averaged densities well above the Greenwald limit n_{GW} [6]. If this property can be conserved in more collisionless plasmas, it is a very attractive feature for burning plasmas.

In discharges at medium densities ($< 0.45n_{GW}$), the value of the power threshold for L-H transitions is not influence by $n = 2$ magnetic perturbations. At intermediate densities ($< 0.65n_{GW}$) type-III ELMs develop right after the L-H transition and at even higher density the field perturbations lead to a threshold power which is at least a factor

of 2 above the usual value. This increase is caused by a flattening of the ion and electron pressure gradients [35].

4. L to H-mode transitions

The studies of the power threshold for L to H-mode transitions and the search for the physically relevant parameters for this transition have been continued. The L-H power threshold dependence on density is well-known to be non-monotonic and exhibits a minimum at a density of about $4 \times 10^{19} \text{ m}^{-3}$ in ASDEX Upgrade [36]. This behavior is schematically indicated in Fig. 3 by the orange region. As power is increased at constant density, the plasma often transitions from L to H-mode through an intermediate phase (I-phase) which exhibits an oscillatory behavior of the edge turbulence and the flow. The figure depicts previous and recent data where geodesic acoustic modes (GAMs) appear in Ohmic and L-mode plasmas and shows regions where turbulence-flow oscillation have been observed in the I-phase [37]. At a line-averaged density of $\bar{n} \approx 4 \times 10^{19} \text{ m}^{-3}$ the heating power required for the transition is minimum. In the low-density range, strong zonal-flow activity was observed previously and the I phase with zonal-flow turbulence oscillations was limited to this region. This is an indication that the Reynolds stress could play an important role in providing the required $E \times B$ shear flow to stabilise the turbulence and trigger the transition. In recent experimental campaigns, the signatures of the I phase were also observed at higher density in the regions marked by the coloured bars.

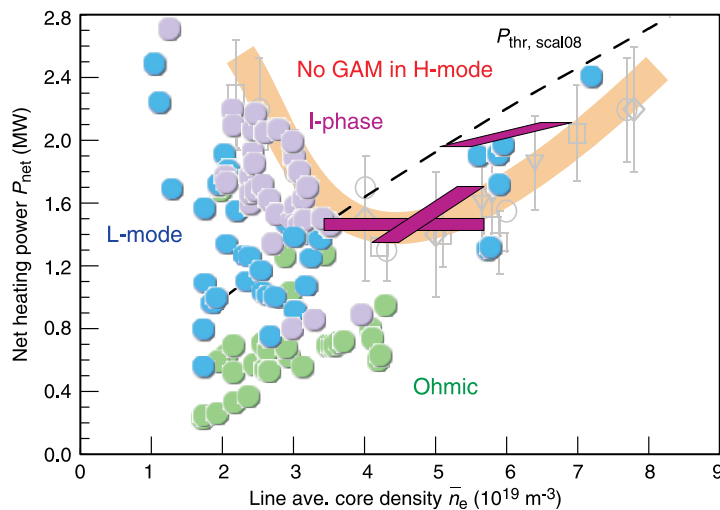


Figure 3. Shaded orange area and grey data points indicate the power threshold for L-H transitions as function of line-averaged density on ASDEX Upgrade. Blue and green symbols indicate GAM oscillation measured by Doppler reflectometry in L-mode and Ohmic discharges, respectively. Purple points and areas indicate regions where the I-phase was observed on. (Adapted from Ref. [37, 38].)

With the upgraded ECRH power it is now possible to study L-H transitions at low density in more detail. Due to strong heating in the electron channel the roles of the

electron and ion temperatures in the transition could be disentangled [8]. It was found that the ion pressure gradient plays the key role. This points to the neoclassical radial electric field and the related flow shear as the important player in the L-H transition. The parameter which orders best between L and H-mode phases is found to be related to the ion pressure gradient in the form $\nabla p_i / en_i$, where n_i is the main ion density. If the minimum of this quantity in the pedestal is plotted as function of the density a horizontal line separates L and H-mode phases [8], as it can be seen in Fig. 4. Since the neoclassical radial electric field in the simplest approximation for a tokamak plasma is given by the term $E_r^{neo} = \nabla p_i / en_i$, this finding revives the interest in the role of the neoclassical $E \times B$ flow shear in the H-mode transition, as it was also stressed in Ref. [39]. In developed H-modes, charge-exchange spectra of different impurities (He^{2+} , B^{5+} , C^{6+} , Ne^{10+}) were analyzed and yielded consistent results for the radial electric field which also agreed with the simple neoclassical prediction [10]. Whether the neoclassical $E \times B$ flow provides the seed flow shear needed to initiate Reynolds stress drive, which then causes the transition, or whether it is itself sufficient to suppress turbulence remains an important question to be addressed in the future.

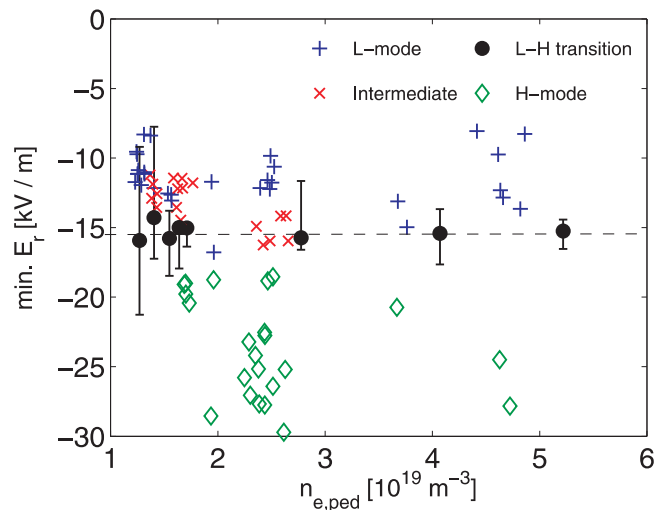


Figure 4. Simple estimated of the neoclassical radial electric field as function of the edge density for different confinement regimes. (Adapted from Ref. [8].)

At medium density and for a number of different heating powers, the edge plasma parameters at the times of the L-H and the H-L transitions were compared [8, 9, 40]. Although L-H and H-L transitions happen at different densities, no strong sign of a hysteresis in the electron pressure was found. Both transitions happen at very similar values of the electron pressure at the plasma edge. In these transient phases radial electric field measurements do not have sufficient time resolution. But since at edge densities above $2 \times 10^{19} \text{ m}^{-3}$ electron and ion temperatures are closely coupled, the electron parameters were used to derive the ion-pressure gradient. In both directions of the transition the estimated ion-pressure gradient assumes values close to the critical

one of Fig. 4 and, therefore, the radial electrical field can be expected to be close to the neoclassical value. Although the L-H and H-L transitions happen at similar values of the edge ion pressure gradient, the values of the electron temperature and density were quite different between forth and back transition [41]. Another interesting observation is that, when the external gas feed is switched off, the final density to which the plasma develops after the transition into H-mode is closely linked to the neutral pressure in the divertor and hence to the neutral particle reservoir stored in the divertor [40].

5. Plasma-wall interaction

Studies related to the divertor and to plasma-wall interaction have been emphasized. The limitation of the divertor heat load is a main concern for future devices. It is closely linked to the power-decay length in the scrape-off layer (SOL) and an accurate prediction of it for ITER and DEMO is of great importance. Since first principle modeling of power and particle exhaust is not available yet, for predictions one has to rely on scaling expressions.

Using improved infra-red camera systems with high spatial and temporal resolution, it was found that previous ELM-averaged measurements [42] overestimate the power decay length. This is due to two reasons: (i) ELM and inter-ELM phases correspond to different physical processes which cannot be scaled in the same way and (ii) the strike line is found to move between ELMs. With these issues resolved on ASDEX Upgrade and JET discharges, an improved scaling expression for the power decay length at the divertor entrance for ELM and inter-ELM phases became available [12]:

$$\lambda_q = 0.73 \times B_{tor}^{-0.78} q_{cycl}^{1.20} P_{SOL}^{0.10} R_{geo}^{0.02} \quad (1)$$

ITER will be operated at similar values of the safety factor q_{cycl} as the discharges used for the scaling. For the prediction to ITER, the important dependence is the one on the magnetic field strength B_{tor} which leads to a reduction in λ_q compared to the values found in present-day devices. Only a weak dependence on the power flux into the SOL, P_{SOL} , and virtually no dependence on the major plasma radius R_{geo} is found. The experimental scaling shows very similar parameter dependencies as a heuristic model where drifts are used to explain the broadening of the decay length in the SOL [12]. For ITER parameters the regression yields a rather short power decay length of $\lambda_q \approx 1$ mm. Unlike for confinement scalings, where the ITER prediction lies about a factor of 10 away from the underlying data, the ITER power decay length is only a factor of two shorter than that in JET. It is important to note, however, that expression (1) is obtained for attached divertor conditions. In more realistic scenarios for a burning plasma closer to the density limit with a partially detached divertor, broader decay lengths can be expected. Also in the high-performance discharges presented in Sec. 1, the power decay length widens substantially with respect to the scaling value. This is shown in Fig. 5, where discharges with attached and partially detached divertor operation are compared. Using radiative cooling the power load is substantially reduced in spite of the doubled heating power.

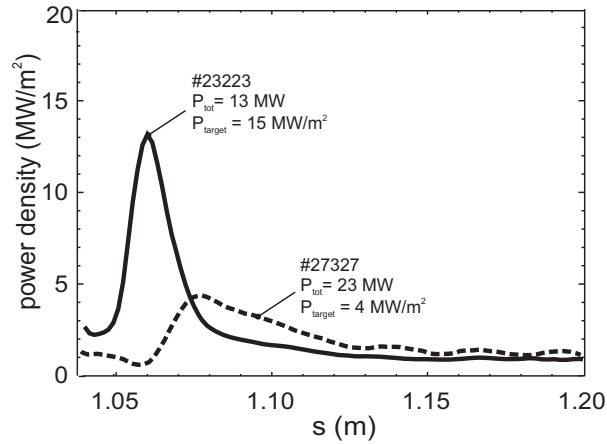


Figure 5. Power density on the divertor plates for attached (#23223) and partially detached (#27327) discharges.

The understanding of the processes leading to power and particle detachment of the divertor target plates in current devices is rather incomplete and a reliable prediction for the divertor behavior of future large scale devices is presently out of reach. For example, the fundamental observation that the detachment of the inner divertor appears much earlier than in the outer divertor is not reproduced by the most sophisticated simulation codes, such as SOLPS5.0. In order to overcome this deficiency, experimental observations with 2D information on the plasma parameters in the divertor are required. To this end, new diagnostics have been installed on ASDEX Upgrade. From 25 lines of sight and with a time resolution of 2.65 ms, the electron density in the inner divertor volume was spectroscopically determined for the first time from Stark broadening of the D_ϵ line. In addition, radiative fluctuations were measured with a new array of fast diode bolometers which cover the inner divertor volume also with a grid of crossed lines of sight [14].

The divertor detachment on ASDEX Upgrade has been studied in Ohmic and L-mode discharges using density ramps up to the density limit, but similar observations are also made in discharges where detachment is initiated by radiative cooling using nitrogen injection. In the L-mode discharges, between 400 and 900 kW of ECRH power was applied. With increasing density it was observed that the divertor undergoes different distinct states and the behaviors of the inner and the outer divertor were found to be strongly coupled. Prior to the detachment of the outer divertor, strong fluctuations in the radiated power appear in the SOL of the inner divertor close to the X-point. The frequency is in the kHz range and scales with the ion mass as $m_i^{-1/2}$. Simultaneously, a high-density region appears in the inner far SOL and around the X-point. During this phase, the experimentally measured particle flux in the inner divertor remains well below the prediction of a two-point model. A high degree of detachment at the inner divertor appears already in an early phase of the density ramp. On the other hand the roll-over in the particle flux at the inner and outer divertor appear at similar densities. After the disappearance of the fluctuations, detachment occurs along the entire inner

target plate.

With tungsten as the plasma facing material, in the divertor volume high density is correlated with high total radiation. Therefore the tomographic reconstruction of the emission measured along the line of sight of the foil bolometers can be used to study the 2D temporal density evolution. Thus it was found that after detachment of the inner strike point a high density region is located at the target plate next to the X-point. This region then moves radially inwards and then closer to the separatrix above the X-point. Simultaneously, the outer divertor completely detaches [14]. The modeling of these observation is ongoing [15].

6. SOL-turbulence studies

For a fundamental description of the power decay length, the understanding of turbulent transport in the scrape-off layer has to be improved. The fluctuations in the SOL are known to be strongly intermittent and large events, called blobs (in 2D) or filaments (in 3D), radially transport plasma as far as to the plasma facing components. The erosion of wall material by the plasma blobs is of great concern for ITER [43].

Advance turbulence simulation codes for the plasma edge and also for the SOL are available. In order to validate these codes, the characteristics of the turbulence needs to be measured in detail and in order to estimate the erosion rate on the first wall, the plasma parameters inside the blobs need to be known. These topics have been addressed in ASDEX Upgrade using different kinds of electric probes.

Fluctuation measurements have been carried out using Langmuir probes close to the separatrix of L-mode discharges [18]. Since the plasma potential and its cross-phase to the density fluctuations is of key importance for a comparison with theory, the plasma potential was directly measured with an emissive probe. In addition, a conditional sampling technique was used to compile current-voltage probe characteristics from which the full set of electron plasma parameters could be deduced inside of blobs. Both methods yielded consistent information on the plasma-potential fluctuations. They were found to be in phase with the density fluctuations as deduced from the ion-saturation current (see Fig. 6a). The plasma-potential fluctuations are, however, out of phase by 180° from the directly measured floating-potential fluctuations (Fig. 6c). The difference between plasma and floating potential fluctuations is caused by electron-temperature fluctuations (Fig. 6b). The temperature fluctuations are also in phase with the density fluctuations and they reverse the amplitude of the floating potential fluctuations with respect to the plasma potential. This emphasizes the known problem related to the measurement of quantities which depend on cross-phases such as turbulent transport or Reynolds stress with Langmuir probe arrays.

A detailed comparison of the fluctuation measurements with gyro-fluid simulations from the GEMR code [44, 45] was carried out [18]. The simulated volume encompasses the transition from close to open field lines including a sheath model for the SOL. In the analyzed region close to the separatrix, simulation and experiment are in excellent

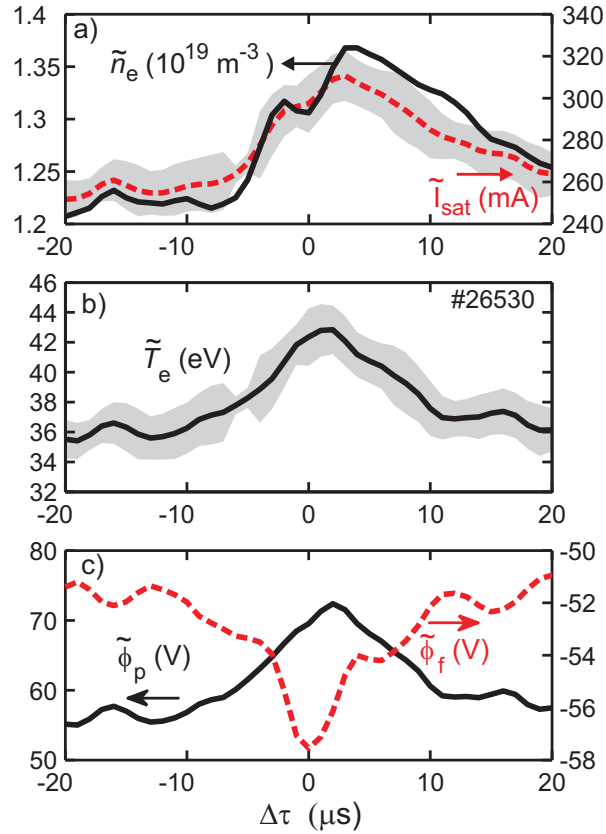


Figure 6. Fluctuating plasma parameters in a blob from conditional sampling. Adapted from Ref. [18].

agreement. Both consistently find in-phase fluctuations in density, plasma potential and electron temperature which is in agreement with a mixing-length approach. Also in the code, where synthetic Langmuir probes have been included, the ion-saturation current measurements turn out to reproduce density fluctuations quite well. As in the experiment, the fluctuations in the floating potential, however, are strongly influenced by temperature fluctuations and, hence, are strongly distorted compared to the actual plasma-potential fluctuations. The fact that both experiment and simulation show that plasma-potential and density fluctuations are almost in phase clearly points to drift waves as the dominant turbulence mechanism in the L-mode edge and near-SOL plasma. Details of the blob generation close to the separatrix are studied and it is observed that an admixture of interchange characteristics increases, i.e. a growth of a bipolar potential structure due to the curvature drift, as the blob propagates radially outward [18].

In order to estimate sputter yields related to the interaction of turbulent filaments or blobs with the plasma facing components and to develop models for the blob dynamics with predictive capabilities, the ion density and temperature inside of the blobs need to be measured. Using a radially movable retarding-field analyser, RFA, and again conditional sampling techniques, a systematic study of the ion energy in turbulent events has been carried out in the SOL of ASDEX Upgrade [19, 20]. Inside of the

plasma filaments which were created by ELM crashes, the RFA measured rather high ion temperatures of up to 200 eV in the far scrape-off layer. The measured ion temperatures amount to values between 5 and 50% of the ion temperature at the pedestal top. The temperature was found to scale with the total energy drop induced by the ELM. Large ELMs seem to carry, on average, ions with higher energy into the far SOL than smaller ones. This might suggest that filaments from larger ELMs propagate faster radially.

Radial propagation velocities of 500 – 2000 m/s were estimated from the temperature decay as function of the distance from the separatrix using a simple blob model [46]. From the measured ion temperature together with densities deduced from the ion-saturation current, parallel power fluxes could be estimated and they were found to agree quite well with thermographic measurements using an IR camera viewing the RFA.

Also the blobs occurring during inter-ELM phases were found to transport high ion temperatures over large radial distances into the SOL. The ion temperature decreases with a radial decay length of about 2 cm and blobs with higher density show also a somewhat higher ion temperature. With increasing distance from the separatrix, the temperature decays faster with radius pointing to reduced radial propagation velocities.

7. Core transport studies

Core momentum and particle transport have been studied over a wide range of plasma parameters. Taking advantage of the enhanced ECRH capabilities, core transport was studied in discharges without an external source of particles or momentum [17]. Using charge-exchange spectroscopy, a comprehensive database of toroidal flow measurements in Ohmic, ECR and ICR-heated L and H-mode discharges could be assembled. In spite of the absence of an external momentum source, a large variation of the flow velocity in the plasma core from co to ctr. direction was measured. In addition, it was observed that in all scenarios the central toroidal Mach number closely correlates with the normalized velocity gradient calculated at about mid plasma radius. The observed variations in the intrinsic rotation velocity at zero external momentum input clearly point to substantial changes in the terms governing the radial momentum transport. Assuming a fixed value for the diffusive component of the transport equation implies the existence of a term leading to transport in direction of the flow gradient. This could be a convective or/and a Reynolds stress term.

Furthermore, the database also exhibits a correlation between the normalized density gradient at about half radius with the velocity gradient and thus to the central rotation velocity. This is shown in Fig. 7a, which also includes some H-mode discharges. In a previous study, core density peaking in the absence of a particle source was successfully described by transport coefficients derived from linear calculations with the gyro-kinetic model GS2 [47, 48]. Using the same code and an adjusted constant tilting angle of -0.3 rad of the turbulent eddies with the experimental parameters as input, the momentum transport and thus the toroidal flow profile can be predicted. Figure 7b

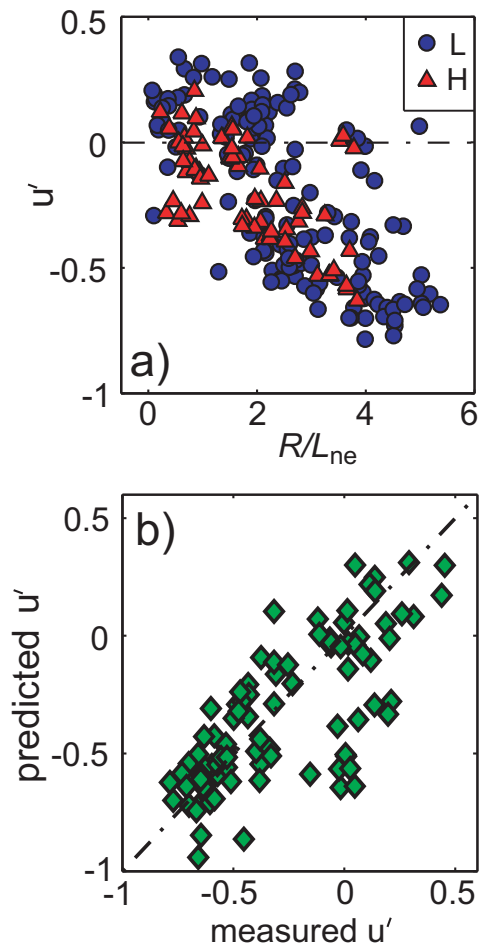


Figure 7. Top: measured density gradient length vs. normalized rotation gradient, bottom: predicted vs. measured rotation gradient. Adapted from Refs. [16, 17].

shows the good agreement between experiment and model predictions. According to that model, all points in the database falling into the trapped-electron-mode (TEM) regime are well described by the modification of the internal momentum transport which is caused by changes in the residual stress through a density gradient dependence. The pinch term plays a minor role only.

A similar behaviour of momentum transport was found in NBI-heated discharges, too. With NBI heating, central particle and momentum sources are present and due to almost equal electron and ion temperature profiles, the discharge core is in the ion-temperature-gradient (ITG) driven turbulence regime. The addition of 2 MW of ECRH to the 2.5 MW of NBI power leads to an increase in electron temperature and to a transition into the TEM regime. According to recent theoretical studies [49] this transition enhances the turbulent particle pinch and indeed a central peaking of the density profile was found. At the same time the rotation profile flattens which is qualitatively consistent with the observations from the internal-rotation database [50]. A comprehensive study of particle transport in the core plasma can be found in Ref. [51].

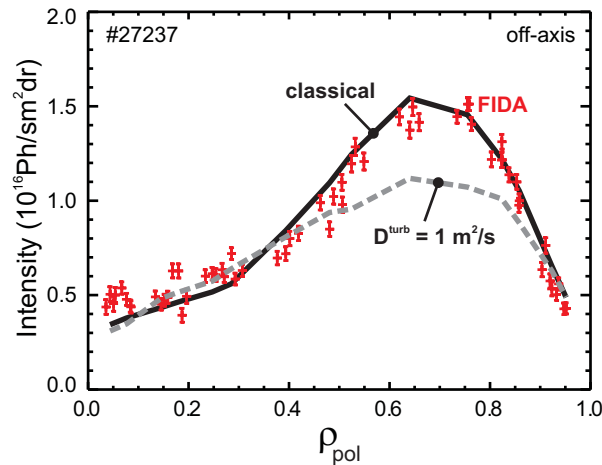


Figure 8. Radial FIDA intensity profiles from a off-axis NBI-heated discharge compared with simulations using classical slowing down and diffusion (solid line) or a diffusion coefficient of $1 \text{ m}^2/\text{s}$ (dashed). Adapted from Ref. [52].

In principle, turbulence could also influence the radial fast ion distribution in the plasma core as generated by NBI. This is of interest for future devices when α -particle heating becomes important. Recently, fast-ion D-alpha (FIDA) spectroscopy, which analyses the Doppler shifted Balmer- α radiation from neutralised deuterium ions, was used to measure the radially resolved slowing-down distribution function of fast ions originating from NBI [53]. The fast-ion profiles from on and off-axis neutral beam sources measured with the FIDA diagnostic were compared with slowing-down ion distribution functions which were calculated with the TRANSP transport code. As depicted in Fig. 8), for the 93 keV beam excellent agreement of the distribution of ions with energies in the range 30 – 60 keV is found when classical slowing down and classical diffusion are used in the calculation which works without any adjustable parameters. In contrast, assuming an anomalous diffusion of $1 \text{ m}^2/\text{s}$ for the fast ions in the TRANSP simulations yields fast ion profiles which are in variance with the experimental result [53]. Therefore, anomalous diffusion of fast ions [54] cannot explain the low current drive efficiency of the off-axis case.

- [1] D. Wagner *et al.*, Nucl. Fusion **48**, 54006 (2008).
- [2] J. Stober *et al.*, EX/1-5, 24th IAEA Fusion Energy Conference (San Diego, U.S.A., 2012).
- [3] W. Suttrop *et al.*, Phys. Rev. Lett. **106**, 225004 (2011).
- [4] W. Suttrop *et al.*, 27th Symposium on Fusion Technology (Liège, Belgium, 2012), sub. J. Nuclear Materials.
- [5] V. Bobkov *et al.*, EX/5-19, 24th IAEA Fusion Energy Conference (San Diego, U.S.A., 2012).
- [6] P. T. Lang *et al.*, Nucl. Fusion **52**, 023017 (2012).
- [7] P. Lang *et al.*, EX/P4-01, 24th IAEA Fusion Energy Conference (San Diego, U.S.A., 2012).
- [8] P. Sauter *et al.*, Nucl. Fusion **52**, 012001 (2012).
- [9] F. Ryter *et al.*, EX/P4-03, 24th IAEA Fusion Energy Conference (San Diego, U.S.A., 2012).
- [10] E. Viezzer *et al.*, High-accuracy characterization of the edge radial electric field at ASDEX Upgrade, subm. to Nucl. Fusion.
- [11] A. Kallenbach *et al.*, Nucl. Fusion **52**, 122003 (2012).
- [12] T. Eich *et al.*, Phys. Rev. Lett. **107**, 215001 (2011).

- [13] T. Eich *et al.*, *ITR/1-1*, 24th IAEA Fusion Energy Conference (San Diego, U.S.A., 2012).
- [14] S. Potzel *et al.*, *Characterization of the Fluctuating Detachment State in ASDEX Upgrade*, 27th Symposium on Fusion Technology (Liège, Belgium, 2012), sub. J. Nuclear Materials.
- [15] M. Wischmeier *et al.*, *EX/P5-34*, 24th IAEA Fusion Energy Conference (San Diego, U.S.A., 2012).
- [16] C. Angioni *et al.*, *Phys. Rev. Lett.* **107**, 215003 (2011).
- [17] R. McDermott *et al.*, *EX/2-1*, 24th IAEA Fusion Energy Conference (San Diego, U.S.A., 2012).
- [18] B. Nold *et al.*, *New J. Phys.* **14**, 063022 (2012).
- [19] M. Kocan *et al.*, *Nucl. Fusion* **52**, 023016 (2012).
- [20] M. Kocan *et al.*, *EX/P7-23*, 24th IAEA Fusion Energy Conference (San Diego, U.S.A., 2012).
- [21] R. Neu *et al.*, *Physica Scripta* **T138**, 14038 (2009).
- [22] R. Neu *et al.*, 27th Symposium on Fusion Technology (Liège, Belgium, 2012), sub. J. Nuclear Materials.
- [23] J. Santos *et al.*, *Nucl. Fusion* **52**, 32003 (2012).
- [24] M. Reich *et al.*, First results of closed loop feedback control of NTMs at ASDEX Upgrade, 39th EPS Conference & 16th Int. Congress on Plasma Physics, Stockholm, 2012.
- [25] G. Pautasso *et al.*, Massive gas injection from the high field side of ASDEX Upgrade, 38th EPS Conference on Plasma Physics, Strasbourg, France, 2011.
- [26] W. A. Suttrop *et al.*, *Europhysics Conference Abstracts* **36F**, P2.092 (2012).
- [27] F. Sommer *et al.*, *Nucl. Fusion* **52**, 114018 (2012).
- [28] A. Kallenbach *et al.*, *Plasma Phys. Controll. Fusion* **52**, 055002 (2010).
- [29] H. Höhnle *et al.*, *Nucl. Fusion* **51**, 083013 (2011).
- [30] W. Suttrop *et al.*, *EX/3-4*, 24th IAEA Fusion Energy Conference (San Diego, U.S.A., 2012).
- [31] M. Garcia-Munoz *et al.*, *EX/6-03*, 24th IAEA Fusion Energy Conference (San Diego, U.S.A., 2012).
- [32] Y. Feng *et al.*, *Contrib. Plasma Phys.* **44**, 57 (2004).
- [33] T. Lunt *et al.*, *Nucl. Fusion* **52**, 054013 (2012).
- [34] H. W. Müller *et al.*, *Europhysics Conference Abstracts* **35G**, P4.122 (2011).
- [35] F. Ryter *et al.*, *Nucl. Fusion* **52**, 114014 (2012).
- [36] F. Ryter *et al.*, *Nucl. Fusion* **49**, 062003 (2009).
- [37] G. Conway *et al.*, *Phys. Rev. Lett.* **106**, 65001 (2011).
- [38] G. Conway *et al.*, presented at TTF Workshop, Padua 2012.
- [39] U. Stroth, P. Manz, and M. Ramisch, *Plasma Phys. Controll. Fusion* **53**, 24006 (2011).
- [40] M. Willensdorfer *et al.*, *Nucl. Fusion* **52**, 114026 (2012).
- [41] E. Wolfrum *et al.*, *Plasma Phys. Controll. Fusion* **54**, 124002 (2012).
- [42] A. Herrmann *et al.*, *J. Nucl. Mater.* **4**, 759 (2003).
- [43] R. Pitts *et al.*, *J. Nucl. Mater.* **415**, S957 (2011).
- [44] S. J. Zweben *et al.*, *Phys. Plasmas* **16**, 82505 (2009).
- [45] A. Kendl, B. Scott, and T. Ribeiro, *Phys. Plasmas* **17**, 072302 (2010).
- [46] W. Fundamenski *et al.*, *Plasma Phys. Controll. Fusion* **48**, 109 (2006).
- [47] M. Kotschenreuther, G. Rewoldt, and W. Tang, *Comp. Phys. Comm.* **88**, 128 (1995).
- [48] E. Fable, C. Angioni, and O. Sauter, *Plasma Phys. Controll. Fusion* **52**, 015007 (2010).
- [49] C. Angioni *et al.*, *Nucl. Fusion* **51**, 023006 (2011).
- [50] R. M. McDermott *et al.*, *Plasma Phys. Controll. Fusion* **53**, 124013 (2011).
- [51] C. Angioni *et al.*, *Plasma Phys. Controll. Fusion* **51**, 124017 (2009).
- [52] B. Geiger, Fast-ion transport studies using FIDA spectroscopy at the ASDEX Upgrade tokamak, 2013, PhD thesis, LMU Munich, IPP Garching, to be published.
- [53] B. Geiger *et al.*, *Europhysics Conference Abstracts* **36F**, P4.068 (2012).
- [54] S. Günter *et al.*, *Nucl. Fusion* **47**, 920 (2007).